J. Fluid Mech. (2002), *vol.* 472, *pp.* 283–305.
DOI: 10.1017/S0022112002002197 Printed in the United Kingdom

Concentration measurements downstream of an insoluble monolayer front

By MICHAEL J. VOGEL AND AMIR H. HIRSA

Department of Mechanical, Aerospace, and Nuclear Engineering
Rensselaer Polytechnic Institute, Troy, NY 12180, USA

(Received 9 April 2001 and in revised form 11 June 2002)

The surfactant concentration distribution on a planar uniform flow with a surface-piercing barrier was measured via the nonlinear optical technique of second-harmonic generation. The measurements were performed for an insoluble surfactant monolayer on the air/water interface. A theoretical model balancing surface elasticity and bulk shear at the interface was developed to predict the concentration profile for any insoluble monolayer. Measured equations of state, relating the surface tension to the surfactant concentration, were used in the model along with velocity data obtained using boundary-fitted digital particle image velocimetry. Theoretical concentration profiles were in agreement with experimental results. Additionally, global predictions from the model for four different insoluble surfactant systems also showed agreement with experimental measurements.

1. Introduction

Monomolecular films (monolayers) on gas/liquid interfaces have received much renewed attention, in part due to observations of self-assembled structures (Wang, Robertson & Gast 1999). This growing interest in monolayers is driven in part by their numerous potential applications, which include coating technologies, chemical and biological sensors, and optoelectronic devices.

Surfactant monolayers have been studied extensively in the presence of flow. Although the concentration distribution of a monolayer along the gas/liquid interface has been predicted for many different flow geometries (e.g. Stone & Leal 1990; Quintana, Cheh & Maldarelli 1992; Bel Fdhila & Duineveld 1996; Eggleton, Pawar & Stebe 1999; Lopez & Hirsa 2000), direct measurements have yet to appear in the literature. Recent developments in nonlinear optics have made such measurements realizable for some flow geometries and monolayers.

The flow studied here has a simple geometry that is suitable for both experiments and theory. As shown schematically in figure 1, when a uniform flow, U_∞, parallel to the gas/liquid interface encounters a surface barrier in the presence of an insoluble monolayer, the monolayer will become compressed against the barrier. At equilibrium, there can exist a monolayer front which delineates an upstream surfactant-free region from a downstream region covered by the monolayer which has a concentration profile, $c(x)$. The coupling of the bulk flow with the interface will cause the monolayer to become essentially stagnant, resembling the no-slip boundary condition of a solid wall. Thus, a boundary layer is formed with its origin essentially coincident with the monolayer front (Harper & Dixon 1974). The sudden fluid deceleration at the leading edge of the boundary layer produces a surface deformation, commonly referred to as

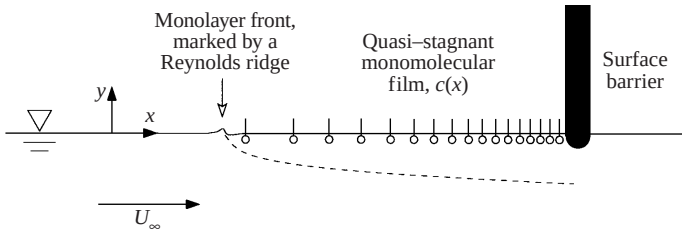

FIGURE 1. Schematic of the flow. Note that the coordinate system origin, here shown displaced to the left for clarity, is coincident with the boundary layer origin.

a Reynolds ridge. Although this deformation is relatively small in amplitude (order 10–100 microns), its curvature makes it visible to the naked eye for a range of flow conditions. A detailed listing of the literature on this flow can be found in Scott (1982). However, the majority of those studies have focused on the Reynolds ridge, which is a very small portion of the monolayer, whereas the present interest is in the entire film.

No experimental measurements of the surfactant concentration distribution have been reported, but Mackros & Krone (1968) measured the surface tension profile using a du Noüy ring tensiometer. The shortcoming of these measurements is that the du Noüy ring method is designed for measurements in quiescent systems. Furthermore, many of the existing experimental studies were performed using tap water and other materials that introduce surface-active contaminants into the system. These generally unidentified (soluble) surfactants make it difficult to reproduce the results of such experiments or to draw conclusions about the structure of the monolayer (Sellin 1968; Mockros & Krone 1968; McCutchen 1970; Scott 1982).

In theoretical models, the concentration of the monolayer can be obtained as part of the solution to the full flow problem. The theoretical models involve a balance at the interface between the surface tension gradient and the bulk shear stress evaluated at the interface. Downstream of the monolayer front, the shear stress has been assumed to be the Blasius solution for flow over a flat plate (McCutchen 1970; Harper & Dixon 1974). One of the drawbacks of the theoretical studies is that idealized equations of state (e.g. linear relation between surfactant concentration and surface tension) have been utilized. Recently it has been shown that the nonlinearity in the equations of state for actual monolayer systems can have a significant influence on the monolayer concentration distribution along the surface (Pawar & Stebe 1996; Johnson & Borhan 1999; Lopez & Hirsa 2000; Hirsa, Lopez & Miraghaie 2001*a*). Another important issue regarding the theoretical models is that many assumptions are made that are not observed to be exactly true in practice (Scott 1982). Examples of such assumptions include a monolayer front that is everywhere perpendicular to the flow and a monolayer that is perfectly stagnant. The present paper aims at providing experimental results on the composition of the full monolayer which can be compared to theoretical models.

For the present measurements, non-invasive laser techniques are utilized for the direct measurement of surfactant concentration distribution along the surface, as well as for the interfacial velocity and bulk shear evaluated at the interface. The nonlinear optical method of second-harmonic generation (SHG) is used for measurement of the surfactant concentration at the air/water interface (Vogel *et al.* 2001). For the interfacial velocity measurements, a variation of the conventional digital particle image velocimetry (DPIV; Willert & Gharib 1991) technique is utilized, referred to as boundary-fitted DPIV (BFDPIV; Hirsa, Vogel & Gayton 2001*b*).

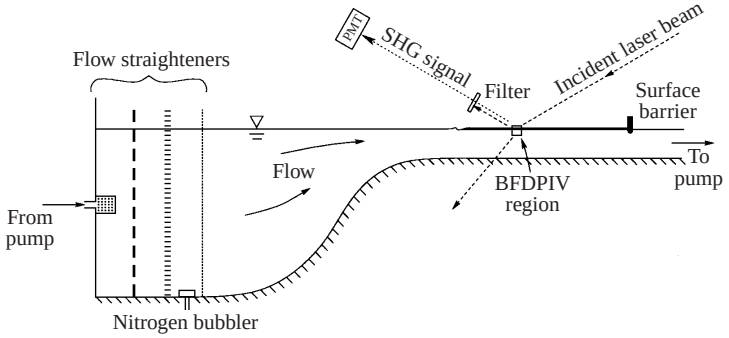

FIGURE 2. Schematic of the channel and the laser beam used to measure surfactant concentration and fluid velocity. Note that the beam is scanned along the monolayer for the measurements.

SHG is a nonlinear spectroscopic technique where a laser beam, incident on a monolayer, induces excitations in the surfactant molecules, causing emission of photons with a frequency twice that of the incident photons (Shen 1989; Corn & Higgins 1994). As a result of the conservation of linear momentum, this second-harmonic signal travels on a path that coincides with the reflected source beam, which makes the removal of the original frequency and measurement of the second-harmonic signal straightforward with the proper filters and detector. SHG is particularly useful since the intensity of its signal is proportional to the square of the concentration of the surfactant molecules. However, the constant of proportionality is strongly dependent on the particular molecule, making SHG practical for only some monolayers.

Recently, simultaneous SHG and BFDPIV measurements were made at the Reynolds ridge (Vogel *et al.* 2001). However, that limited region is not sufficient to draw general conclusions about the underlying physics of the entire monolayer. Here, a similar experimental setup has been used to examine the full monolayer and its interaction with the bulk flow.

The details of the experimental setup, including the channel geometry, measurement techniques, and material preparation, are presented in the following section. Surface velocity and shear measurements are given in § 3 along with SHG measurements of monolayer concentration. In § 4, a theoretical model is developed which permits the calculation of the concentration profile using a stress balance similar to those described above. Also, concentration profile calculations and global predictions of the model are compared to experimental measurements.

2. Experimental apparatus

The measurement instruments and the design of the flow channel have been described by Vogel *et al.* (2001). Here a brief discussion of the relevant details and refinements necessary to study the full monolayer are presented.

2.1. *Flow*

A free-surface channel with uniform flow was used in the experiments. The channel was constructed of inert materials and covered to minimize contamination from the atmosphere. The channel, shown in figure 2, was a pump-driven closed flow loop with a constant 10.3 cm width. All experiments were conducted at speeds smaller than 23.2 cm s^{-1} to prevent the capillary–gravity surface waves that form at higher

	$U_\infty = 6.0\,\mathrm{cm\,s^{-1}}$		$U_\infty = 18.0\,\mathrm{cm\,s^{-1}}$	
	Vertical plane	Horizontal plane	Vertical plane	Horizontal plane
Spatial	0.014	0.010	0.009	0.010
Temporal	0.010	0.012	0.013	0.011

TABLE 1. Spatial and temporal uniformity in the test section in the absence of a monolayer, given as u_{rms}/u_{avg}. The measurements are taken across the channel away from the boundary layers over a period of 6 s.

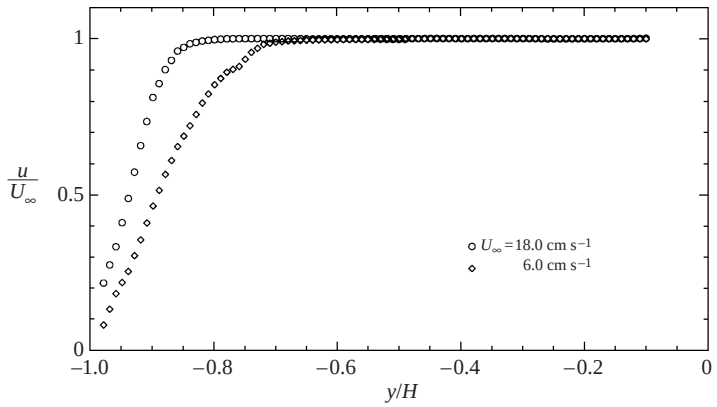

FIGURE 3. Flow uniformity measurements in the channel: u-velocity profiles in the (x, y)-plane in the absence of a monolayer measured via conventional DPIV (velocity errors: $\pm 1\%$ of full scale). Because the orientation of the camera was perpendicular to the sidewalls for conventional DPIV measurements, the region near the air/water interface ($y/H = 0$) was obstructed by thin Teflon strips which are used to prevent surfactant molecules from adsorbing to the glass.

velocities (McCutchen 1970; Lighthill 1978). Also, experiments were performed at a temperature of $22.5 \pm 0.5\,^{\circ}\mathrm{C}$.

The two-dimensional contraction, which follows a series of flow straighteners, was designed to minimize non-uniformities in the flow as well as stationary waves on the air/water interface. The test section was 61 cm long and filled to a constant water depth of $H = 4.5$ cm for the present experiments. The leading edge of the monolayers observed in these experiments was always at least 10 cm from the inlet of the test section. The surface-penetrating barrier was constructed of Teflon and was interference fitted into the test section to prevent monolayer leakage. The semicircular bottom of the barrier (radius 0.3 cm) was inserted to a depth of 0.3 cm as illustrated in figure 1.

Measurements of flow uniformity in the test section were made with a conventional DPIV setup and are shown in figure 3. These measurements were made in a vertical plane at the midpoint (spanwise and streamwise) of the test section. These data, normalized with the depth and free-stream velocity, are a time-average over 6 s. The boundary layer at the floor of the test section can be clearly seen for both flow speeds shown. These experiments were performed without a monolayer, so no shear layer is observed at the air/water interface.

Comprehensive measurements of spatial and temporal uniformity of the flow in the test section for the vertical as well as the horizontal plane are presented in table 1.

The flow was analysed using the data away from the boundary layer (i.e. in the range $-0.65 < y/H < -0.10$; see figure 3). The data for both the spatial and temporal uniformity are presented as the r.m.s. (about the mean) normalized by the mean value. The data show that the flow non-uniformities are typically about 1%, which is of the same order as the uncertainty in the DPIV measurements.

2.2. *BFDPIV and SHG measurement systems*

The interfacial velocity and vertical shear were measured using boundary-fitted digital particle image velocimetry (BFDPIV) and the monolayer concentration was measured using second-harmonic generation (SHG). Experiments have been previously performed in which BFDPIV and SHG measurements were taken simultaneously using the same laser beam (Vogel *et al.* 2001), with the transmitted portion of the incident beam providing the illumination for BFDPIV (see figure 2). Simultaneity may be valuable for unsteady or non-repeatable flows. However, simultaneous measurements require compromising both techniques: SHG measurement requires a small beam footprint of low power density from an unmodified beam so that the signal has a high spatial resolution and yet does not photo-bleach the monolayer; on the other hand, BFDPIV requires a larger area of illumination and high laser power for sufficient particle illumination. The steady and repeatable nature of the present flow allows the two measurements to be performed at different times, which permits the optimization of each signal.

In BFDPIV (Hirsa *et al.* 2001*b*), total internal reflection at the air/water interface is used to determine the surface location in the images of the seeded flow. The velocity field is then determined at precise locations relative to the surface. This allows measurements of interfacial velocity and shear which, in general, are not possible with the conventional DPIV technique due to its failure to apply any special treatment to the interface (Lin & Perlin 1998; Tsuei & Savaş 2000; Hirsa *et al.* 2001*b*). The BFDPIV technique has been applied at the Reynolds ridge (Vogel *et al.* 2001) and the measured surface deformation was found to be in agreement with both theoretical results (Harper & Dixon 1974) and experimental measurements (Scott 1982; Warncke, Gharib & Roesgen 1996). Although the interface is essentially flat over much of the region of interest of this flow, its precise location is still needed for accurate determination of interfacial velocity and shear via BFDPIV.

For all the BFDPIV measurements presented below, a pair of Nd:YAG lasers was utilized to permit arbitrary time delay between successive video frames. The two laser beams were made essentially collinear and the combined beam and all the optics (including the BFDPIV camera) were traversed along the x-axis for the entire length of the monolayer. The beam was passed through a series of lenses for reshaping and focusing. The typical field of view for the measurements at the surface was 0.41 (in the direction of flow) by 0.28 cm.

The SHG measurements were made using a single Nd:YAG laser beam which was also traversed along the centre of the channel, although the scanning range for SHG was limited to monolayers of lengths less than 30 cm. No beam reshaping was performed for SHG, as a high degree of coherence is a requisite for adequate signal-to-noise ratio. Before reaching the surface, the polarity of the incident laser beam was rotated and made uniform to optimize the signal (Judd 1996). Immediately before reaching the surface, the beam was band-pass filtered to eliminate any spurious light at the second-harmonic frequency. After reflecting from the surface, the beam, which consists of both the incident frequency and the reflected second-harmonic frequency, passed through filters which removed the incident frequency. A

photomultiplier tube then collected the second-harmonic signal which was ultimately recorded by a computer.

In order to process the SHG data, a calibration curve relating the monolayer concentration to the SHG signal was needed. An *in situ* calibration curve was obtained in a Langmuir trough (Gaines 1966) constructed of Teflon which was specifically designed to fit inside the test section of the drained channel. The trough was fitted with an optical window that allowed the transmitted laser beam to pass through the trough without generating heat or any second-harmonic signal from the Teflon floor. The trough was equipped with an electrobalance for Wilhelmy plate measurements of surface tension.

2.3. *Water and monolayer preparation*

Special care is necessary to keep the air/water interface clean because water is especially prone to contamination. Due to the relatively large volume of water required for each experiment (50 l), commercial distilled water (Poland Springs) was used since its residual surfactant level has been shown to be comparable to doubly distilled water produced in the lab, both of which are considerably cleaner than commercial HPLC-grade water (Hirsa *et al.* 2001*a*). The present SHG measurements made on the commercial distilled water surface were also found to be similar to those on the doubly distilled water for cases with and without a monolayer. The difference in the average signals and the standard deviations of the signal over time between the two types of water were within 7% of each other for each case. The seeding particles used for BFDPIV measurements were cleaned to remove excess surfactants by the technique given in Vogel *et al.* (2001). The particles were also shown to have no effect on the SHG signal or on the cleanliness of the system as indicated by the development of a monolayer front, described below.

The channel was cleaned with HPLC-grade methanol which was allowed to evaporate prior to several rinses with distilled water. Liquid nitrogen boiloff was emitted from a glass diffuser before each experiment, which aided in bringing background surfactants to the surface where they could be easily cleaned (Merson & Quinn 1965; Scott 1975). With the surface barrier in place and water flowing through the channel, any residual surfactants at the interface were trapped against the surface barrier, forming a monolayer which can grow in time. A completely surfactant-free system on the scale of the present apparatus is essentially impossible to attain, but conditions have been consistently obtained where the monolayer, marked by a Reynolds ridge, is only 1–2 cm in length (approximately 5% of the typical deposited monolayer length) after thirty minutes of flow, which is a long period of time relative to the duration of an experiment. This length of the film due to the residual contamination (1–2 cm) is also small compared to previously reported values, namely 80 cm for tap water (Mockros & Krone 1968), 5–6 cm for de-ionized (DI) water and 3 cm for treated DI water (Mockros & Quinn 1965). The measurement reported by Mockros & Krone is for $U_\infty = 10\,\mathrm{cm\,s^{-1}}$, similar to the present case ($U_\infty = 12$–$15\,\mathrm{cm\,s^{-1}}$). Merson & Quinn do not provide a direct measure of U_∞ corresponding to their reported film length, but their data show that the length is only a weak function of U_∞.

The surfactants studied here, selected for their wide range of behaviour, are all insoluble in water: hemicyanine (Sigma-Aldrich, product number 36683-8), stearic acid (26838-0), vitamin K_1 (28740-7), and oleyl alcohol (O-8880). The equations of state for these monolayers on water were found to be repeatable and to show various limiting behaviours at large concentration, discussed below (§ 4). Two of the monolayers (hemicyanine and stearic acid) exhibit measurable surface (shear) viscosity

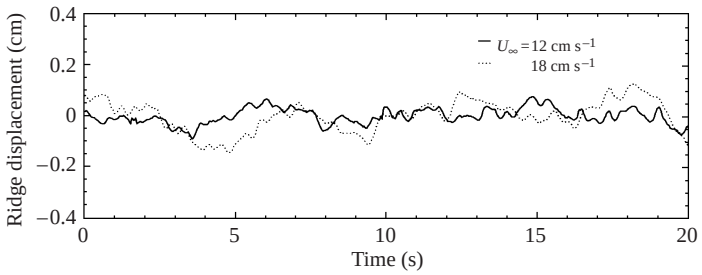

FIGURE 4. Variation in monolayer length, measured by displacement of the Reynolds ridge over time for two different bulk velocities (displacement error: ±2.5%).

whereas the other two (vitamin K_1 and oleyl alcohol) are essentially inviscid over a wide range of concentrations. These behaviours are consistent with their bulk phase at room temperature: hemicyanine and stearic acid are solid while vitamin K_1 and oleyl alcohol are liquid. Additionally, hemicyanine is a dye molecule (Gaines 1987) which gives a strong SHG signal (Girling *et al.* 1985, 1987; Kajikawa, Takezoe & Fukuda 1991), and was used in this study for that reason. There are ample data in the literature for these monolayers (hemicyanine: Young *et al.* 1989; Hall *et al.* 1993; Hirsa *et al.* 1997; stearic acid: Gaines 1966; Poskanzer & Goodrich 1975; Saylor & Handler 1999; vitamin K_1: Weitzel, Fretzdorff & Heller 1956; Gaines 1966; Hirsa *et al.* 2001*a*; oleyl alcohol: Gaines 1966; Hirsa & Willmarth 1994; Mass & Milgram 1998).

Surfactants were diluted in a high-purity volatile solvent to a concentration of 1.0 g l^{-1} to aid in measurement and spreading on the air/water interface: chloroform for hemicyanine, hexane for vitamin K_1, and benzene for both oleyl alcohol and stearic acid. The general procedure used for depositing a monolayer is a standard one (Gaines 1966). Specifically, individual drops of surfactant solution were added every five seconds near alternating ends of the test section using a microsyringe (10, 25 or 100 µl, depending on the total volume of solution) until the required amount was deposited. Once the monolayer was spread and allowed to equilibrate, the flow in the channel was started slowly, analogous to a slow compression of the monolayer in the Langmuir trough (§4). Additional details about the flow startup procedure are given in Vogel *et al.* (2001). For the present experiments involving concentration distribution measurements, the uniformity of the spread monolayer was verified by performing an SHG scan over the surface before flow was initiated.

Although the average location of the Reynolds ridge is essentially constant over time, the exact location fluctuates by a small amount on short time scales as shown in figure 4. It should be noted that the monolayer front displacements shown in the figure are very small compared to the total length of the monolayer (of order 1 : 300). This fluctuation is consistent with the velocity fluctuations in the test section, reported in table 1. The effect of these fluctuations on the measured vertical shear and surfactant concentration are negligible, as shown below.

3. Experimental results

3.1. *Flow results*

The results of the BFDPIV measurements are presented in figure 5. These measurements were made for two of the surfactants, hemicyanine and vitamin K_1, at

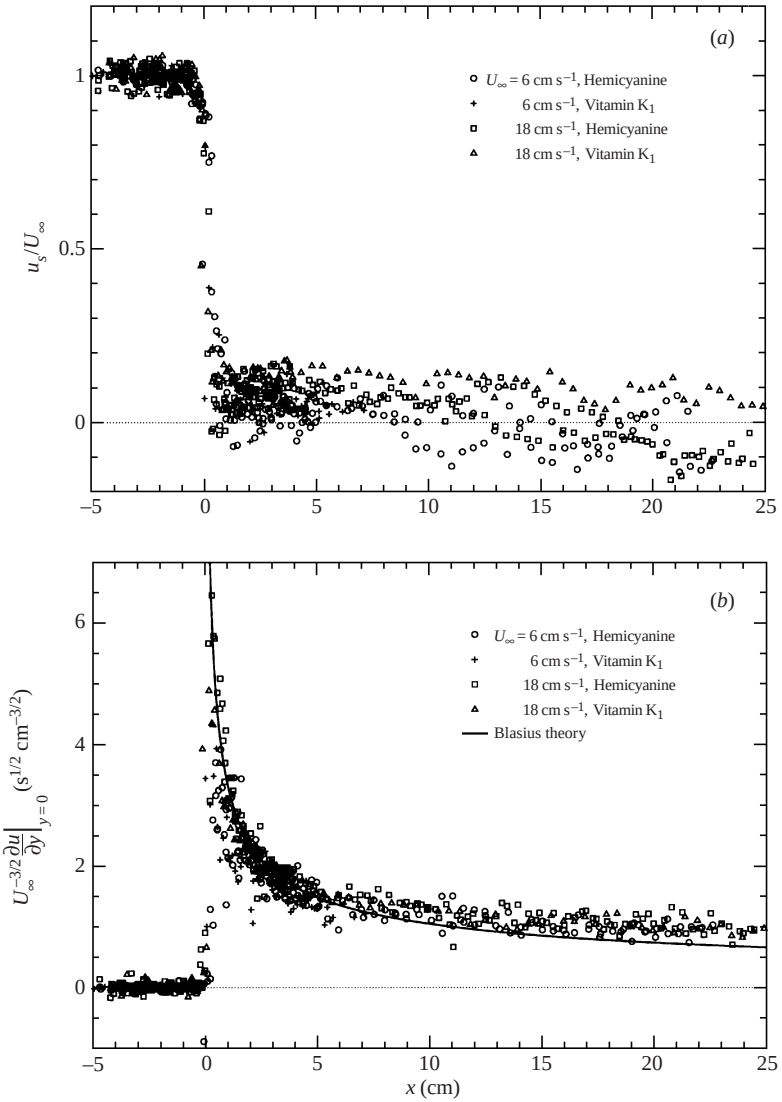

FIGURE 5. Measured (BFDPIV) (*a*) interfacial velocity and (*b*) vertical shear evaluated at the interface for two different surfactants and two different flow speeds. Velocities in (*a*) have been normalized by the free-stream velocity, U_∞, and the shear in (*b*) has been scaled by $U_\infty^{3/2}$, as per the Blasius solution. Dotted lines at zero are shown for reference (interfacial velocity and shear errors: $\pm 5\%$ of full scale).

two different free-stream velocities. For each monolayer deposited, two scans along the centreline of the channel were made with the measurement probe: one of low resolution over the entire monolayer and one of high resolution near its leading edge where gradients are large. The repeatability of the experiment was established by a second set of scans for hemicyanine. Each data point in the figure was obtained by averaging the data in one-third of an image captured by the camera (consisting of $33/3 = 11$ interrogation windows), which corresponds to a spatial resolution of 0.14 cm. The amount of surfactant deposited for each monolayer was chosen so that

the monolayer length was nominally 30 cm for all cases except for the 18 cm s^{-1} vitamin K_1 scan, due to monolayer collapse (described in § 4).

Normalizing the interfacial velocity by U_∞ in figure 5(*a*) shows that the profiles are invariant to the type of surfactant and the free-stream velocity. All of the interfacial velocities, u_s/U_∞, are essentially uniform upstream of the monolayer front except for a slight decrease in the region $-1 < x < 0$ cm, probably due to the diffusion of vorticity (Carrier & Lin 1948; Harper 1992). This is immediately followed by an abrupt transition to low velocities. After the sudden decrease, the velocities for all the cases are close to zero. It is important to realize that in the downstream region, fluctuations that appear are primarily temporal, as these data points were taken over the scanning period of 50 s. The slight two-dimensionality of the interfacial flow (discussed below) along with the fluctuations in the bulk flow may contribute to the noise in the u_s data, although the former is expected to be the larger effect since the fluctuations of velocity upstream of the monolayer are smaller than the fluctuations downstream. It should also be noted that this scatter in surface velocity is not consistently seen in the vertical shear measurements at the interface, $\partial u/\partial y|_{y=0}$, shown in figure 5(*b*). Since the shear and not the interfacial velocity is directly used in the stress balance, the velocity fluctuations do not influence the theoretical analysis (§ 4).

The shear data in figure 5(*b*) have been scaled by $U_\infty^{3/2}$, based on the Blasius solution for flow over a flat plate. As expected, the surface is shear-free upstream of the monolayer front. At the front, there is a sudden jump in shear, followed by a decay that resembles the shear at a flat solid wall. It should be noted that the surface vorticity caused by the curvature at the monolayer front (Reynolds ridge) has been shown to be significantly smaller than the shear measured at the interface (Warncke *et al.* 1996; Vogel *et al.* 2001). As with the interfacial velocity profiles, the shear does not appear to be a function of the type of surfactant or the free-stream velocity. It can be seen from the general agreement for $1 < x < 6$ cm with the Blasius solution, also shown in figure 5(*b*), that the monolayers act similarly to an immobile surface despite the small amount of surface velocity measured. However, at larger x, the measured shear at the monolayer is significantly larger than the Blasius solution (by more than 40%, which is outside the error bounds). The validity of this measured deviation is indirectly confirmed by the results shown in § 4. The reason for the difference between the measured shear and the Blasius solution is not clear, although it is not altogether surprising considering the differences between this flow and a theoretical solid wall: (i) surface deformation (Reynolds ridge) near the leading edge, (ii) monolayer diffusivity, which is also strongest near the leading edge, (iii) curvature of the monolayer front (in the x, z-plane), which is due to the finite span of the channel, and (iv) non-zero surface-normal vorticity and the corresponding recirculating flow of the monolayer. Based on the results of Carrier & Lin (1948) and Harper (1992), special treatment of the singularity at the leading edge has a minimal effect on the solution far from the leading edge, so the leading edge effects (i–iii) are not expected to be responsible for the large discrepancy observed at large x (>6 cm) in the present results. Thus, the most important difference between the present flow and the solid wall is that here there is finite surface-normal vorticity, as vortex lines can terminate at the interface, which could cause the surface-parallel component to be different from that at a solid wall. The occurrence of surface-parallel vorticity (z-direction) larger than that at a solid wall has been predicted in theoretical studies (Tryggvason *et al.* 1992; Tsai & Yue 1995). The relation between surface-parallel and surface-normal vorticity was considered recently for an axisymmetric flow (Lopez & Hirsa 2000).

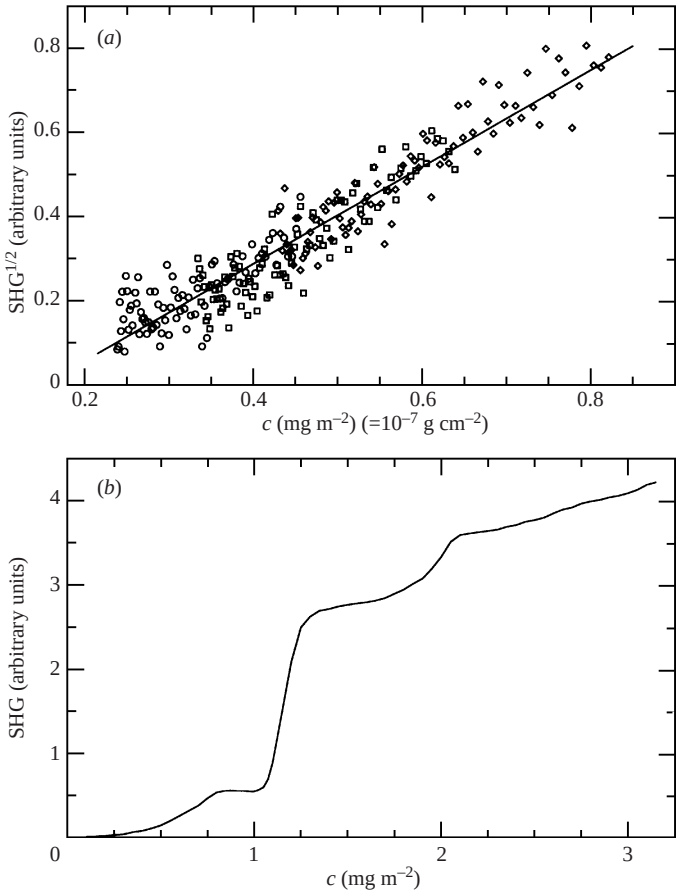

FIGURE 6. Calibration curve obtained for converting SHG signal to surfactant concentration for hemicyanine. (*a*) At low concentration, the measurements show the expected theoretical linear relationship between the square root of the SHG signal and concentration. (*b*) The best-fit curve over the full range of the calibration curve used. Note that over a narrow range (≈ 0.8–$1.0\,\mathrm{mg\,m^{-2}}$), c is a multi-valued function of the SHG signal (measurement error discussed in the text).

3.2. *SHG results*

Validation of the SHG technique is presented in figure 6, which shows the measured calibration curve used to convert SHG data to concentration values for hemicyanine. SHG theory (idealized) predicts proportionality between the square-root of the SHG signal and the concentration of the surfactant molecule at the interface. This is confirmed for $c < 0.8\,\mathrm{mg\,m^{-2}}$ in figure 6(*a*). Each data point is a 50-bin average of the SHG signal (30 Hz) with a 50% overlap with the adjacent point. To obtain the full range of concentrations for the calibration curve, several quasi-static compressions (shown by different symbols in figure 6*a*) were necessary because of the limited compression ratio of the Langmuir trough. The slow speed of the moving barriers ($0.05\,\mathrm{cm\,s^{-1}}$) allows the monolayer sufficient time to equilibrate and prevents the resulting data from being a function of the compression rate. To ensure repeatability, all of the compressions had a 50% overlap with their adjacent cases. The repeatability shown in these measurements establishes that the carefully deposited monolayers

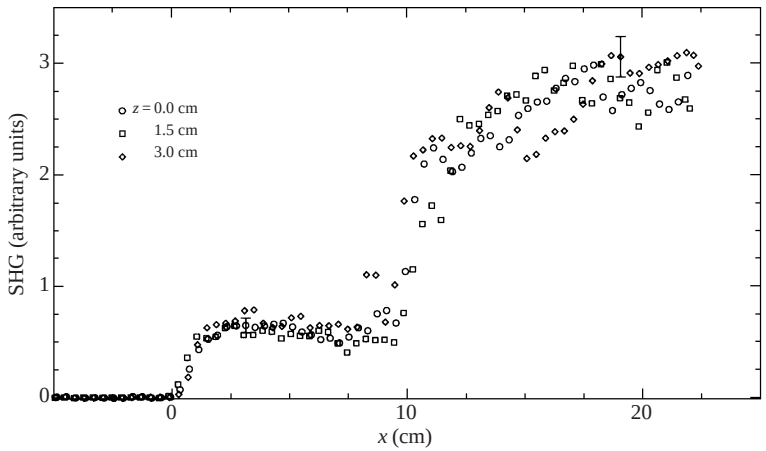

FIGURE 7. Measurements of SHG signal along the x-axis for three different spanwise locations at fixed $U_\infty = 15 \pm 0.2\,\mathrm{cm\,s^{-1}}$. Representative error bars are shown for two concentrations.

behave similarly regardless of initial concentration. Other validating tests of the SHG signal can be found in Vogel *et al.* (2001).

Figure 6(*b*) shows the best-fit curve for the SHG calibration over the full rage of concentration. For $c > 0.8\,\mathrm{mg\,m^{-2}}$, phase transitions and other complications with hemicyanine monolayers cause a departure from the $\mathrm{SHG}^{1/2} \propto c$ prediction. These deviations have been previously observed (Frysinger 1992; Barnoski-Serfis 1994). There is a narrow region of the calibration curve where the concentration is a multi-valued function of the SHG signal. However, none of the data points subsequently presented fell in this small range of SHG signal, although the conversion of such a point would be straightforward despite the larger uncertainty involved. The standard deviation of the SHG signal data used to obtain this curve is 0.06 (arbitrary units, see figure 6) for low concentrations, gradually increasing to a maximum value of 0.32 at a concentration of $1.5\,\mathrm{mg\,m^{-2}}$, and then decreasing to a value of 0.18 for concentrations above $2.5\,\mathrm{mg\,m^{-2}}$. The error in measured concentration (obtained via the standard curve) is a strong function of the concentration due to the shape of the standard curve. Relatively high errors occur where the SHG signal is a weak function of concentration.

When a monolayer is trapped on a uniform flow in a channel of finite width, it has been shown that the monolayer is not completely stagnant, but rather a circulatory flow pattern is present where the maximum velocity is typically an order of magnitude smaller than the free-stream velocity (Kenning & Cooper 1966; Scott 1982; Warncke Lang & Gharib 2000). Figure 7 shows that there is no measurable effect on the concentration distribution from the unsteadiness or three-dimensionality of the flow. The figure shows that the concentration distribution is essentially the same for three different spanwise locations from the centreline ($z = 0\,\mathrm{cm}$) up to $z = 0.6$ times the half-channel-width. In order to minimize the uncertainty, raw SHG data are presented in the figure instead of the concentration values obtainable through the calibration curve. It should be noted that the multi-valued region of the calibration curve causes the decreasing trend in the SHG signal in the region $3 < x < 8\,\mathrm{cm}$, so a corresponding decrease in concentration does not necessarily occur. All subsequent scans presented were performed along the centre of the channel ($z = 0$).

Figure 8 shows the effect of varying the total surfactant mass deposited for a fixed

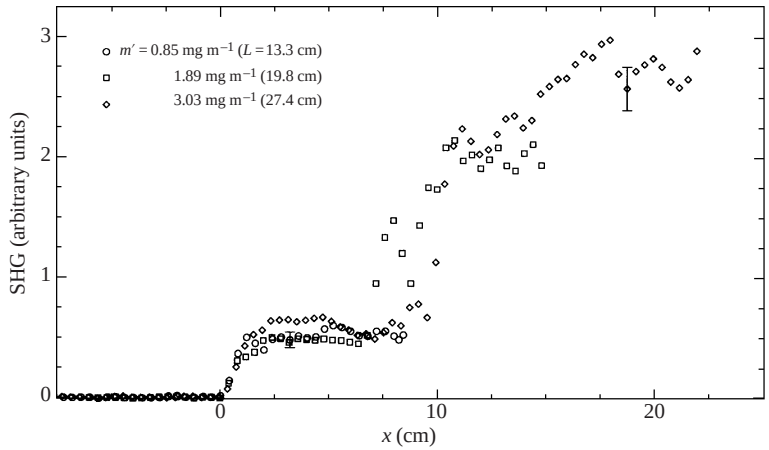

FIGURE 8. Measurements of SHG signal along the x-axis down the centre of the channel ($z = 0$) for $U_\infty = 15 \pm 0.2\,\mathrm{cm\,s^{-1}}$. Each scanned monolayer has a different total mass of surfactant. Representative error bars are shown for two concentrations.

free-stream velocity. Since it has been established that the concentration profile is independent of z, the value of the total surfactant mass is subsequently given as mass per unit span of the channel (m') to make the results more general. In the figure, raw SHG data are presented for the same reason given for figure 7. Due to the angle of the incident beam and the portion of the surface barrier that extends above the air/water interface, the 5–6 cm of the monolayer closest to the barrier (e.g. $22 < x < 27.4\,\mathrm{cm}$ for $m' = 3.03\,\mathrm{mg\,m^{-1}}$) could not be probed.

For the various initial concentrations, it can be seen that the SHG profiles, and therefore concentration profiles, are essentially identical (to within the experimental uncertainty) up to the length of the respective monolayer. Based on this observation, it can be hypothesized that the total mass of surfactant only determines the length of the monolayer and has no effect on the shape of the concentration profile. Furthermore, the concentration profile shape for a given surfactant must only be a function of the one remaining parameter: U_∞. This hypothesis forms the basis of the present theoretical model.

4. Theoretical model and validations

For a (planar) Newtonian gas/liquid interface in the absence of external forces, the tangential stress balance is between (i) the shear stress in the bulk liquid evaluated at the interface, (ii) Marangoni stress due to surface tension gradients, and (iii) interfacial stress due to surface viscosities (surface shear viscosity and surface dilatational viscosity); see Scriven (1960), Slattery (1990) and Edwards, Brenner & Wasan (1991). The x-component of the stress boundary condition may be written as

$$\mu\left(\frac{\partial u}{\partial y}+\frac{\partial v}{\partial x}\right)=\frac{\partial \sigma}{\partial x}+(\kappa^s+\mu^s)\,\frac{\partial}{\partial x}\left(\frac{\partial u}{\partial x}+\frac{\partial w}{\partial z}\right)+\mu^s\frac{\partial}{\partial z}\left(\frac{\partial u}{\partial z}-\frac{\partial w}{\partial x}\right), \tag{4.1}$$

where all terms are evaluated at the interface. Here μ is the dynamic viscosity of the bulk fluid, u and w are the velocities in the x- and z-directions, and μ^s and κ^s are the interfacial shear and dilatational viscosities, respectively. The first-order correction for a non-planar interface (Edwards *et al.* 1991), $\partial v/\partial x$, is expected to be of order $m^2(\partial u/\partial y)$, where m is the surface slope. The maximum m for this flow is 10^{-2} (Vogel

et al. 2001), which makes this term negligible. Note, this estimate agrees with recent measurements of $(\partial v/\partial x)/(\partial u/\partial y)$ of 10^{-5}–10^{-3} (Hirsa *et al.* 1997).

The weak interfacial circulation pattern of the present monolayer films consists of four symmetric and counter-rotating cells spanning the length of the monolayer. Terms in (4.1) with interfacial viscosities may be neglected for the quasi-stagnant monolayers examined here. This assumption can be justified by considering the large central portion of the monolayer away from the two ends (the Reynolds ridge and the barrier) where w and $\partial/\partial x$ can be neglected. This leaves the leading surface viscosity term in (4.1), $\mu^s(\partial^2 u/\partial z^2)$, which can be shown to be over two orders of magnitude smaller than the values of the two other remaining terms in the stress balance by approximating the interfacial velocity distribution with, for example, a linear or sinusoidal profile across the channel with a maximum velocity of $0.15U_\infty$ (as seen in experiments and verified in figure 5*a*). The interfacial shear viscosity for hemicyanine (one of the more viscous monolayers examined) is approximately $10^{-3}\,\mathrm{g\,s^{-1}}$ at the expected concentration, which gives a value for the surface viscosity term that is 250 times smaller than the values of the Marangoni stress or the bulk shear stress evaluated at the interface. The stress balance can then be written (Johnson & Stebe 1996; Hirsa *et al.* 2001*a*)

$$\mu\frac{\partial u}{\partial y}\bigg|_{y=0} = \frac{\mathrm{d}\sigma}{\mathrm{d}x}. \tag{4.2}$$

To incorporate the surfactant concentration into the stress balance, the elastic term can be rewritten, without loss of generality, via the chain rule:

$$\mu\frac{\partial u}{\partial y} = \frac{\mathrm{d}\sigma}{\mathrm{d}c}\frac{\mathrm{d}c}{\mathrm{d}x}. \tag{4.3}$$

In order to compute the concentration distribution, the stress balance can be discretized as

$$c_{n+1} = c_n + \frac{\mu(\partial u/\partial y)|_{x=x_n}}{(\mathrm{d}\sigma/\mathrm{d}c)|_{c=c_n}}\Delta x. \tag{4.4}$$

The profile, $c(x)$, is computed beginning at the monolayer front, where $x_o = 0$ and $c_o = 0$. The calculations are then marched downstream with values of Δx chosen to keep the Δc small in order to obtain a converged solution. Concentration profiles are computed using curve fits, described below, to the measured equations of state (surface tension as a function of surfactant concentration) and the shear stress at the interface.

The equations of state shown in figure 9 were obtained in the Langmuir trough described in § 2.2. As expected at low concentrations, all of the equations of state are flat with the surface tension equal to that of clean water (Gaines 1966). Vitamin K_1 and oleyl alcohol both show another nearly flat region at high concentrations due to monolayer collapse (Weitzel *et al.* 1956). Beyond the collapse limit, increasing the surfactant concentration will not significantly change the surface tension because the monolayer, unable to accommodate such tight molecular packing, begins to form multilayers (Adamson & Gast 1997). The equation of state for hemicyanine shows inflection points and cusp-like features which indicate various phase transitions, but the monolayer does not appear to reach an absolute lower limit of surface tension in this range of concentration. Stearic acid is qualitatively different from the other monolayers. The drop in surface tension, occurring at a much higher concentration, is much more sudden and steep. Beyond the range shown, the equation of state for

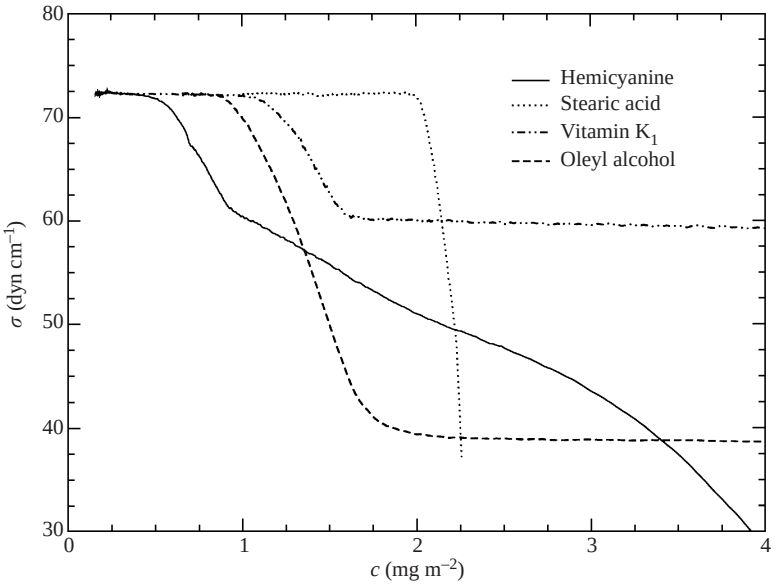

FIGURE 9. Equations of state measured for the four insoluble surfactants (concentration error: $\pm 2.5\%$; surface tension error: $\pm 0.1\,\mathrm{dyn\,cm^{-1}}$).

stearic acid was not repeatable. However, the concentrations encountered in this study were all in the measured range.

A curve fit was found for the measured shear stress for various free-stream velocities (independent of the monolayer material). As shown in figure 5(b), the measured shear is similar to the Blasius solution for $x < 6\,\mathrm{cm}$ but larger for $x > 6\,\mathrm{cm}$. Figure 10(a) shows the fit for the experimental data as well as the Blasius solution, both for $U_\infty = 18\,\mathrm{cm\,s^{-1}}$. The model that was used in fitting the shear data blends a linear profile for low values of x with a modified Blasius solution at higher values of x. This is better than the Blasius solution because it avoids the singularity at the origin (Carrier & Lin 1948; Harper & Dixon 1974; Harper 1992). Due to the deviations between the measured shear and the Blasius solution, the curve fit for the shear stress at the interface includes an arbitrary shape factor, $A(x)$, for the Blasius term:

$$\mu \frac{\partial u}{\partial y}\bigg|_{y=0} = \tau_F = \frac{1}{(1/\tau_L) + (1/\tau_B)A(x)}. \tag{4.5}$$

This fit for the shear stress at the interface, τ_F, has the form of the lens equation which has been suggested for many different applications (Coles 1996). The linear portion of the curve fit, which is dominant at low values of x, is $\tau_L = \mu G x \sqrt{U_\infty}$; the Blasius solution is $\tau_B = \alpha \mu U_\infty^{3/2}/\sqrt{\nu x}$ where α is the constant from the Blasius solution (0.332); and the shape factor is $A(x) = x^{0.685}/(0.65 + 0.5x)$. Here, μ and ν are respectively the dynamic and kinematic viscosities of the bulk fluid and G (= 325) determines the magnitude of the peak shear. Note that all dimensional quantities are in c.g.s. units. The maximum uncertainty in BFDPIV measurements due to the finite resolution of the probe occurs at the monolayer front where the gradients are largest. The effect of changing the peak shear by $\pm 25\%$ (by varying G from 504 to 183) is shown by the shaded region in figure 10(a).

The results of the concentration profile calculations using equation (4.4) with

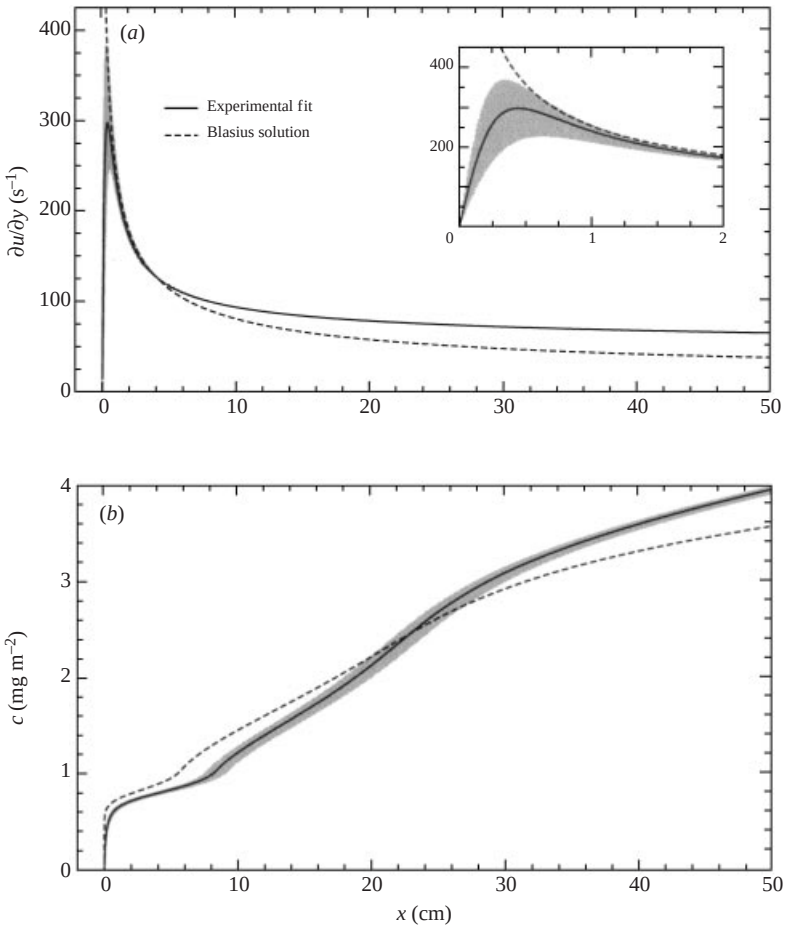

FIGURE 10. (*a*) Different models of surface shear. The shaded region shows the effect of a $\pm 25\%$ error in the measured value of peak shear. (*b*) Theoretical concentration profiles resulting from the different surface shear models in (*a*). Both plots are for a hemicyanine monolayer with $U_\infty = 18\,\mathrm{cm\,s^{-1}}$.

the two different shear models are shown in figure 10(*b*). These predictions of the concentration profile are for a hemicyanine monolayer. Both of the curves show a sudden increase in concentration caused by the relative flatness of the equation of state up to approximately $c = 0.5\,\mathrm{mg\,m^{-2}}$. This rapid increase is followed by a monotonically increasing concentration distribution. The small deviations from a linear increase can be attributed to details of the nonlinearities in the equation of state. For example, both of the concentration profiles show a similar feature at $c = 0.95\,\mathrm{mg\,m^{-2}}$, where the equation of state has a phase transition. The predictions cross at $x = 23\,\mathrm{cm}$ but then begin to diverge with downstream distance. The effect of the uncertainty band for the measured peak shear presented in figure 10(*a*) only weakly affects the overall prediction of the concentration profile, as shown in figure 10(*b*).

Using the experimental fits for the shear stress and the equations of state, theoretical concentration curves were computed over a range of velocities for each surfactant, and the results are shown in figure 11. All of the profiles show a sudden increase in

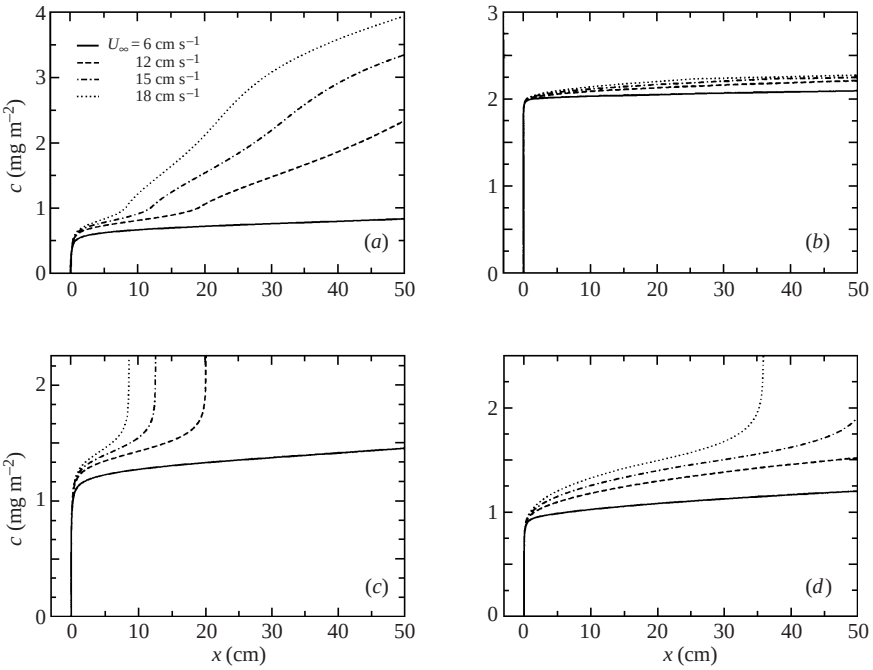

FIGURE 11. Theoretical concentration profiles computed with the present model for a variety of flow velocities and surfactants: (*a*) hemicyanine, (*b*) stearic acid, (*c*) vitamin K_1, (*d*) oleyl alcohol.

concentration at the monolayer front followed by a gradual increase with downstream distance. Generally, slower velocities correspond to smaller shear, which causes the concentration profile to rise along the downstream direction at a slower rate than for higher velocities. The concentration profiles for hemicyanine exhibit a sharp change near $c = 0.95\,\mathrm{mg\,m^{-2}}$, as observed in the previous figure. The steep transition in the equation of state for stearic acid causes the concentration profiles to remain relatively flat and very close to one another. Vitamin K_1 and oleyl alcohol exhibit profiles with sharp changes that asymptote toward infinite concentration, which is an indication of monolayer collapse corresponding to the flatness of the respective equations of state at high concentration. It is interesting to note that all of the concentration profiles resemble the shape of their corresponding equations of state rotated by 90° counterclockwise (with surface tension oriented along the bottom axis and concentration along the vertical axis).

Figure 12 shows theoretical concentration profiles from figure 11 for hemicyanine along with experimental measurements of the concentration profiles obtained via SHG for two different velocities. For the low-velocity case, there is good agreement between the measured points and the calculated curve. Agreement also generally exists for the high-velocity case, although with downstream distance the measured concentration is lower than the theoretical profile by as much as 25%. The uncertainty in the theoretical model which builds up with downstream distance can, in principle, contribute to this discrepancy. More importantly, the difference can be attributed to the increase in measurement uncertainty due to the flatness of the calibration curve in this region of concentration (see figure 6*b*).

The basic theory can be extended to make global predictions of the monolayer which can, in turn, be validated experimentally without direct measurements of

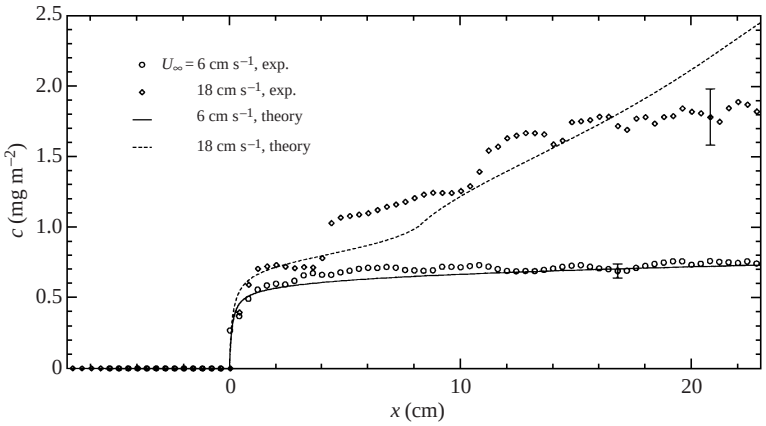

FIGURE 12. Hemicyanine concentration profiles measured by SHG. Also shown are the corresponding theoretical curves from figure 11. Representative error bars are shown (velocity error: $\pm 0.2\,\mathrm{cm\,s^{-1}}$).

concentration. As discussed at the end of § 3.2, for a given surfactant the shape of the concentration profile is only a function of U_∞, so the length of the monolayer is solely determined by the total mass of surfactant present on the interface at the given U_∞. The length of the monolayer can be predicted by applying conservation of mass:

$$m' = \int_0^L c(x, U_\infty)\,\mathrm{d}x, \tag{4.6}$$

where, again, m' is the total mass of surfactant per unit width of the channel, L is the length of the monolayer, and the concentration profile, $c(x, U_\infty)$, has been determined by equation (4.4). Thus, curves of constant m' can be plotted for various U_∞ and L, leading to the creation of U_∞–L–m' families of curves for different surfactants, shown in figure 13. For each point on a curve, the concentration profile (calculated for each value of U_∞) is integrated up to a length, L, which gives the total mass per unit width, m', as prescribed by equation (4.6). The general shapes of the curves show the expected behaviour that, for a monolayer of a given total mass, as the velocity is increased, the monolayer is further compressed, resulting in a smaller value of L. The stearic acid U_∞–L–m' plot has very flat curves of constant m' because of the weak dependence of concentration profile on U_∞ shown in figure 11. The curves for vitamin K_1 and oleyl alcohol show a distinct collapse limit, appearing as nearly overlapping curves of constant m' at larger values of U_∞. In this region, increasing m' will not significantly increase the length of the monolayer. This is due to the asymptotic behaviour of the concentration profiles near the collapse limit.

Note that the global predictions may not at present be generalized for arbitrary surfactant systems and bulk liquids. The shear stress distribution measured along the monolayer may not scale in a universal way for a fluid with viscosity different than that of water. Also, intrinsic interfacial properties such as surfactant diffusivity which may affect shear stress near the monolayer front are generally not known for most systems.

The collapse limit can be estimated analytically by using the Blasius model as a first-order solution of shear stress in equation (4.2). Integrating the left-hand side of the equation with respect to x from $x = 0$ to $x = L_c$, where L_c is the collapse limit

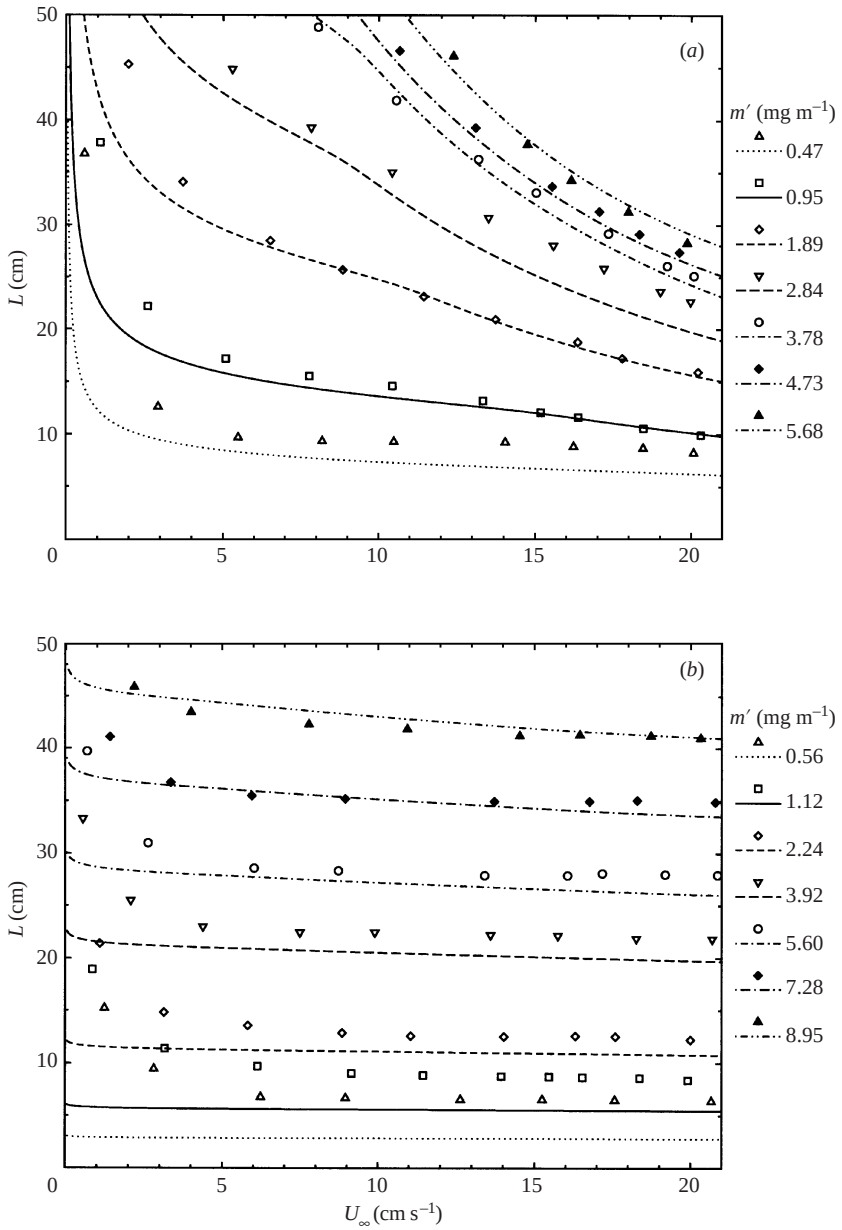

FIGURE 13(*a*, *b*). For caption see facing page.

length, leaves on the right-hand side only the collapse surface tension subtracted from the clean water value, defined as the collapse pressure, $\Pi_c = \sigma_o - \sigma_c$. The collapse pressure can easily be obtained from the equation of state. The integration yields

$$\frac{4(\mu\alpha)^2}{\nu} U_\infty^3 L_c = \Pi_c^2. \tag{4.7}$$

The collapse length is then only a function of the bulk velocity and the collapse pressure and is therefore independent of the shape of the equation of state. These

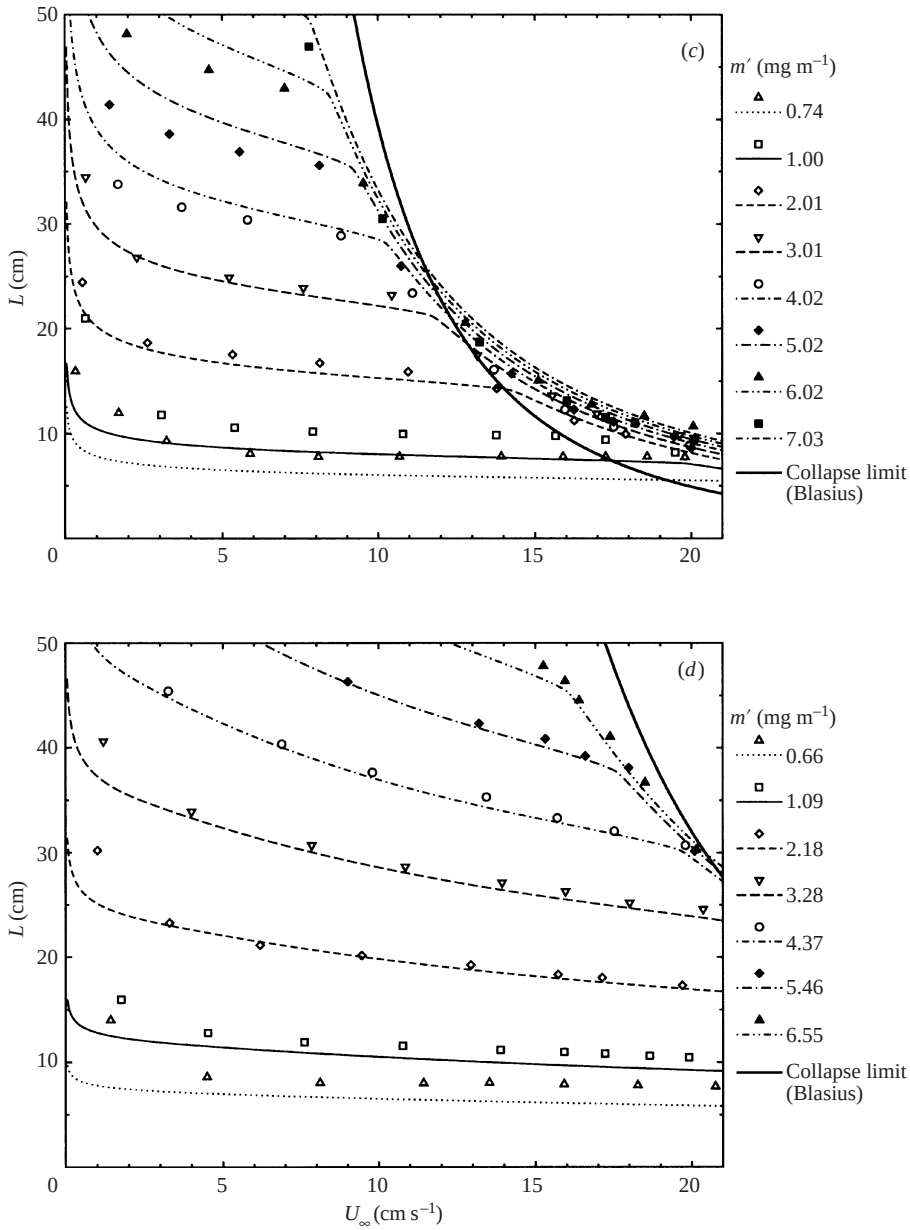

FIGURE 13. Families of U_∞–L–m' curves relating the bulk velocity (U_∞) and monolayer length (L) to the total amount of surfactant per unit width of the channel (m') for (*a*) hemicyanine, (*b*) stearic acid, (*c*) vitamin K_1, (*d*) oleyl alcohol. The points represent experimental data while curves represent theoretical predictions. Parts (*c*) and (*d*) also show the theoretical collapse limits (Blasius) given by equation (4.7) (velocity measurement error: $\pm 3\%$; length error: ± 0.2 cm; surfactant mass error: $\pm 2.5\%$).

theoretical collapse curves, plotted in figure 13(*c*, *d*) for vitamin K_1 and oleyl alcohol, are similar to the collapse limits found by the full computations. The discrepancies are due to the Blasius solution overpredicting the actual shear at small values of x and underpredicting at large x (see figure 10). An interesting result can be obtained

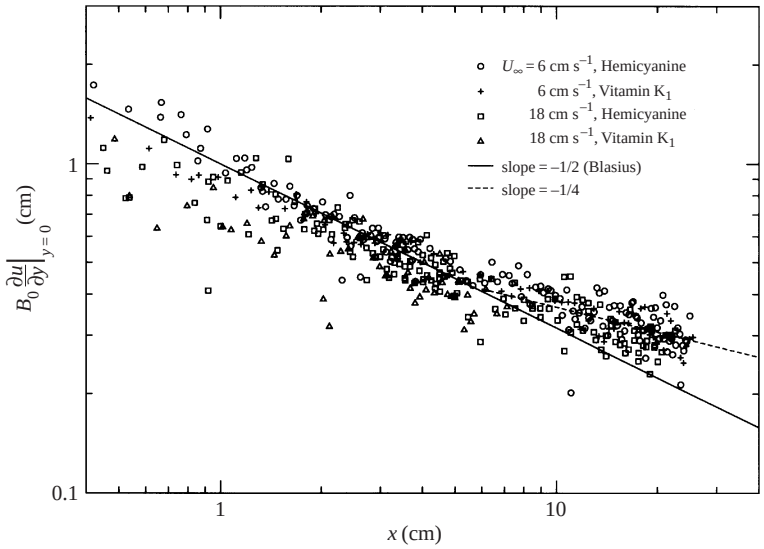

FIGURE 14. Measured (BFDPIV) vertical shear evaluated at the interface for two different monolayers and two different flow speeds. The data are plotted on a log-log scale along with the Blasius solution and an arbitrary curve fit at higher values of x. Note, $B_0 = \frac{2}{0.664}\sqrt{\nu/U_\infty^{3/2}}$.

by substituting the surface tension of clean water for the collapse limit. This can be considered an absolute limiting value for Π_c. Substituting the appropriate values in c.g.s. units into equation (4.7) yields the limit: $L_c < 1.18 \times 10^6/U_\infty^3$. A similar concept of the collapse limit was suggested by McCutchen (1970).

Also shown in figure 13 are experimental measurements. For each set of constant m', the data points correspond to a monolayer that was deposited as described in § 2.3. The leading edge of the monolayer was located using the DPIV system and the free-stream velocity was measured at the same time using an LDV (laser-Doppler velocimeter) system. The agreement between the theoretical U_∞–L–m' curves and the experimental data is good except at small values of L, possibly due to effects from residual surfactants in the channel. Moreover, the agreement in the collapse limits (figure 13c, d) between the measured data points and the full theoretical curves which use the measured stress (as opposed to the approximation which used the Blasius solution) provides a validation of the measured stress and confirms that the Blasius solution away from the leading edge (shown in figure 5b) underpredicts the actual stress.

In order to clarify the measured stress distribution and its relation to the Blasius solution, the data in figure 5(b) were plotted on a log-log scale. Figure 14 shows that the shear stress at the surface follows the Blasius solution ($-1/2$ slope) up to about $x = 6$ cm, after which the data seem to be better fitted by a smaller slope, e.g. $-1/4$. This reduction in slope is not expected to be attributable to turbulence since the maximum Re_x for these data is less than 5×10^4, which is about half of the critical Re for the Blasius solution based on linear theory (Schlichting & Gersten 2000). Furthermore, there is no sign of increased scatter in the measured stress in the region of reduced slope. The fundamental difference between this flow and the rigid wall makes it difficult to speculate on the reasons for the observed change in slope.

5. Concluding remarks

The surfactant concentration distribution of an insoluble monolayer on the surface of a flowing system has been measured and compared to a theoretical model. The non-invasive probing of the monolayer used the nonlinear optical method of second-harmonic generation. The theoretical model used experimentally obtained shear stress at the interface and equations of state which are significantly different from the Blasius solution and linear equations of state previously used (e.g. McCutchen 1970; Harper & Dixon 1974). The concentration profiles and the U_∞–L–m' curves derived from the theoretical model were generally found to be in good agreement with the experiments.

Two-dimensionality and unsteadiness of the interfacial flow were observed, with two-dimensionality being the more important of the two effects. However, these effects were shown to only affect the vertical shear and to have no direct influence on the concentration profile, as shown in figure 7. Furthermore, the general agreement between the predictions and the measurements justifies the assumptions made in the development of the model (e.g. neglecting interfacial viscosity effects). The vertical vorticity and its coupling to the bulk flow and the corresponding two-dimensionality of the monolayer film appear to cause the distribution of parallel vorticity to be different from that of the solid wall case. However, it appears that the manifestation of the vertical vorticity at the surface is weak enough (due to the large length of the monolayer) that the monolayer can be modelled as one-dimensional, whereas its effects in the bulk (vertical shear) must be accounted for. Although the axisymmetric problem has been investigated (Lopez & Hirsa 2000), no full three-dimensional treatment of vortex lines at a surfactant-covered surface has yet been presented.

Finally, it should be noted that measurement techniques similar to those presented here may be applied to other flow geometries. For example, normal shear measurements at curved interfaces (e.g. drops or bubbles) are possible (Lin & Perlin 1998; Tsuei & Savaş 2000; Hirsa *et al.* 2001*b*) and can provide the necessary stress input for a theoretical model to predict monolayer concentration along the interface. Direct SHG measurements of concentration in such geometries are difficult to implement, but not impossible. The techniques can also be applied to more complex flows such as soluble surfactant systems or to monolayers with strong flow in the plane of the interface.

The authors would like to thank the reviewers for their helpful comments. In particular, we would like to thank Professor H. A. Stone for his many useful comments, including the suggestion for including figure 14. The authors would also like to acknowledge Professor G. M. Korenowski and Mr J. S. Kelley of the RPI Chemistry Department for consultation on the SHG setup. This research was funded by the National Science Foundation through grant No. CTS-0116947.

REFERENCES

Adamson, A. W. & Gast, A. P. 1997 *Physical Chemistry of Surfaces*. Wiley–Interscience.

Barnoski-Serfis, A. 1994 Nonlinear optical properties of insoluble monolayers at the air-water interface. PhD thesis, Rensselaer Polytechnic Institute.

Bel Fdhila, R. & Duineveld, P. C. 1996 The effect of surfactant on the rise of a spherical bubble at high Reynolds and Peclet numbers. *Phys. Fluids* **8**, 310–321.

Carrier, G. F. & Lin, C. C. 1948 On the nature of the boundary layer near the leading edge of a flat plate. *Qt. Appl. Maths* **6**, 63–68.

Coles, D. 1996 Turbulent shear flow. *Bull. Am. Phys. Soc.* **41**, 1703.

Corn, R. M. & Higgins, D. A. 1994 Optical second harmonic generation as a probe of surface chemistry. *Chem. Rev.* **94**, 107–125.

Edwards, D. A., Brenner, H. & Wasan, D. T. 1991 *Interfacial Transport Processes and Rheology*. Butterworth–Heinemann.

Eggleton, C. D., Pawar, Y. P. & Stebe, K. J. 1999 Insoluble surfactants on a drop in an extensional flow: a generalization of the stagnated surface limit to deforming interfaces. *J. Fluid Mech.* **385**, 79–99.

Frysinger, G. S. 1992 Nonlinear optical spectroscopy of air/water interface chemistry. PhD thesis, Rensselaer Polytechnic Institute.

Gaines, G. L. 1966 *Insoluble Monolayers at Liquid-Gas Interfaces*. Interscience.

Gaines, G. L. 1987 Photoisomerization of stilazolium chromophores with potential nonlinear optical applications. *Agnew. Chem. Intl Ed.* **26**, 341–342.

Girling, I. R., Cade, N. A., Kolinsky, P. V., Earls, J. D., Cross, G. H. & Peterson, I. R. 1985 Observation of second harmonic generation from Langmuir–Blodgett multilayers of a hemicyanine dye. *Thin Solid Films* **133**, 101–112.

Girling, I. R., Cade, N. A., Kolinsky, P. V., Jones, R. J., Peterson, I. R., Ahmad, M. M., Neal, D. B., Petty, M. C., Roberts, G. G. & Feast, W. J. 1987 SHG in mixed hemicyanine: Fatty acid Langmuir–Blodgett monolayers. *J. Opt. Soc. Am.* B **4**, 950–955.

Hall, R. A., Thistlethwaite, P. J., Grieser, F., Kimizuka, N. & Kunitake, F. 1993 Characterization of hemicyanine aggregates in air–water monolayers. *J. Phys. Chem.* **97**, 11974–11978.

Harper, J. F. 1992 The leading edge of an oil slick, soap film, or stagnant bubble cap in Stokes flow. *J. Fluid Mech.* **237**, 23–32.

Harper, J. F. & Dixon, J. N. 1974 The leading edge of a surface film on contaminated flowing water. In *Fifth Australasian Conf. on Hydraulics and Fluid Mechanics*, pp. 499–505.

Hirsa, A., Korenowski, G. M., Logory, L. M. & Judd, C. D. 1997 Determination of surface viscosities by surfactant concentration and velocity field measurements for an insoluble monolayer. *Langmuir* **13**, 3813–3822.

Hirsa, A. H., Lopez, J. M. & Miraghaie, R. 2001*a* Measurement and computation of hydrodynamic coupling at an air/water interface with an insoluble monolayer. *J. Fluid Mech.* **443**, 271–292.

Hirsa, A. H., Vogel, M. J. & Gayton, J. D. 2001*b* Digital particle velocimetry technique for free-surface boundary layer measurements: application to vortex pair interactions. *Exps. Fluids* **31**, 127–139.

Hirsa, A. & Willmarth, W. W. 1994 Measurements of vortex pair interaction with a clean or contaminated free surface. *J. Fluid Mech.* **259**, 25–45.

Johnson, D. O. & Stebe, K. J. 1996 Experimental confirmation of the oscillating bubble technique with comparison to the pendant bubble method: the adsorption dynamics of 1-decanol. *J. Colloid Interface Sci.* **182**, 526–538.

Johnson, R. A. & Borhan, A. 1999 Effects of insoluble surfactants on the pressure-driven motion of a drop in a tube in the limit of high surface coverage. *J. Colloid Interface Sci.* **218**, 184–200.

Judd, C. J. 1996 Nonlinear optical spectroscopy of the air/water interface. PhD thesis, Rensselaer Polytechnic Institute.

Kajikawa, K., Takezoe, H. & Fukuda, A. 1991 Symmetry and second-order susceptibility of hemicyanine monolayer studied by surface second-harmonic generation. *Japan J. Appl. Phys.* **30**, 1050–1062.

Kenning, D. B. R. & Cooper, M. G. 1966 Interfacial circulation due to surface-active agents in steady two-phase flows. *J. Fluid Mech.* **24**, 293–306.

Lighthill, J. 1978 *Waves in Fluids*. Cambridge University Press.

Lin, H. J. & Perlin, M. 1998 Improved methods for thin, surface boundary layer investigations. *Exps. Fluids* **25**, 431–444.

Lopez, J. M. & Hirsa, A. H. 2000 Surfactant-influenced gas–liquid interfaces: nonlinear equation of state and finite surface viscosities. *J. Colloid Interface Sci.* **229**, 575–583.

Mass, J. T. & Milgram, J. H. 1998 Dynamic behavior of natural sea surfactant films. *J. Geophys. Res.* **103**, 15695–15715.

McCutchen, C. W. 1970 Surface films compacted by moving water: demarcation lines reveal film edges. *Science* **170**, 61–64.

Merson, R. L. & Quinn, J. A. 1965 Stagnation in a fluid interface: properties of the stagnant film. *AIChE. J.* **11**, 391–395.

Mockros, L. F. & Krone, R. B. 1968 Hydrodynamic effects on an interfacial film. *Science* **161**, 361–363.

Pawar, Y. P. & Stebe, K. J. 1996 Marangoni effects on drop deformation in an extensional flow: the role of surfactant physicochemistry. I. Insoluble surfactants. *Phys. Fluids* **8**, 1738–1751.

Poskanzer, A. & Goodrich, F. C. 1975 A new surface viscometer of high sensitivity. II. Experiments with stearic acid monolayers. *J. Colloid Interface Sci.* **52**, 213–221.

Quintana, G. C., Cheh, H. Y. & Maldarelli, C. 1992 The effect of viscoelasticity on the translation of a surfactant covered Newtonian drop. *J. Non-Newtonian Fluid Mech.* **45**, 81–103.

Saylor, J. R. & Handler, R. A. 1999 Capillary wave gas exchange in the presence of surfactants. *Exps. Fluids* **27**, 332–338.

Schlichting, H. & Gersten, K. 2000 *Boundary Layer Theory*. Springer.

Scott, J. C. 1975 The preparation of water for surface-clean fluid mechanics. *J. Fluid Mech.* **69**, 339–351.

Scott, J. C. 1982 Flow beneath a stagnant film on water: The Reynolds ridge. *J. Fluid Mech.* **116**, 283–296.

Scriven, L. E. 1960 Dynamics of a fluid interface. *Chem. Engng Sci.* **12**, 98–108.

Sellin, R. H. J. 1968 Existence of a surface tension discontinuity at a liquid free surface. *Nature* **217**, 536–538.

Shen, Y. R. 1989 Surface properties probed by second-harmonic and sum-frequency generation. *Nature* **337**, 519–525.

Slattery, J. C. 1990 *Interfacial Transport Phenomena*. Springer.

Stone, H. A. & Leal, L. G. 1990 The effects of surfactants on drop deformation and breakup. *J. Fluid Mech.* **220**, 161–186.

Tryggvason, G., Abdollahi-Alibeik, J., Willmarth, W. W. & Hirsa, A. 1992 Collision of a vortex pair with a contaminated free surface. *Phys. Fluids* A **4**, 1215–1229.

Tsai, W. T. & Yue, D. K. P. 1995 Effects of soluble and insoluble surfactant on laminar interactions of vortical flows with a free surface. *J. Fluid Mech.* **289**, 315–349.

Tsuei, L. & Savaş, O. 2000 Treatment of interfaces in particle image velocimetry. *Exps. Fluids* **29**, 203–214.

Vogel, M. J., Hirsa, A. H., Kelley, J. S. & Korenowski, G. M. 2001 Simultaneous measurements of free-surface velocity and surfactant concentration via a common laser probe. *Rev. Sci. Instrum.* **72**, 1502–1509.

Wang, S.-W., Robertson, C. R. & Gast, A. P. 1999 Two-dimensional crystallization of streptavidin mutants. *J. Phys. Chem.* B **103**, 7751–7761.

Warncke, A., Gharib, M. & Roesgen, T. 1996 Flow measurements near a Reynolds ridge. *Trans. ASME: J. Fluids Engng* **118**, 621–624.

Warncke Lang, A. & Gharib, M. 2000 Experimental study of the wake behind a surface-piercing cylinder for a clean and contaminated free surface. *J. Fluid Mech.* **402**, 109–136.

Weitzel, G., Fretzdorff, A.-M. & Heller, S. 1956 Grenzflächenuntersuchungen an tokopherol-verbindungen und am vitamin K_1. *Hoppe-Seylers Z. Physiol. Chem.* **303**, 14–26.

Willert, C. E. & Gharib, M. 1991 Digital particle image velocimetry. *Exps. Fluids* **10**, 181–193.

Young, M. C. J., Jones, R., Tredgold, R. H., Lu, W. X., Ali-Adib, Z., Hodge, P. & Abbasi, F. 1989 Optical and structural characterization of Langmuir–Blodgett multilayers of non-polymeric and polymeric hemicyanines. *Thin Solid Films* **182**, 320–332.